The Impact of the Spectral Tail on the Evolution of the Kurtosis of Random Seas

Barratt, Dylan; van den Bremer, Ton S.; Adcock, Thomas A.A.

DOI
10.1115/1.4055480

Publication date
2022

Document Version
Final published version

Published in
Journal of Offshore Mechanics and Arctic Engineering

The Impact of the Spectral Tail on the Evolution of the Kurtosis of Random Seas

Dylan Barratt
Department of Engineering Science,
University of Oxford,
Oxfordshire, Oxford OX1 3PJ, UK

Ton S. van den Bremer
Faculty of Civil Engineering and Geosciences,
Delft University of Technology,
2628 CD Delft, The Netherlands
e-mail: ton.vandenbremer@eng.ox.ac.uk

Thomas A. A. Adcock[1]
Department of Engineering Science,
University of Oxford,
Oxfordshire, Oxford OX1 3PJ, UK
e-mail: thomas.adcock@eng.ox.ac.uk

We perform simulations of random seas based on narrow-banded spectra with directional spreading. Our wavefields are spatially homogeneous and nonstationary in time. We truncate the spectral tail for the initial conditions at different cutoff wavenumbers to assess the impact of the spectral tail on the kurtosis and spectral evolution. We consider two cases based on truncation of the wavenumber tail at $|\boldsymbol{k}|/k_p = 2.4$ and $|\boldsymbol{k}|/k_p = 6$. Our simulations indicate that the peak kurtosis value increases if the tail is truncated at $|\boldsymbol{k}|/k_p = 2.4$ rather than $|\boldsymbol{k}|/k_p = 6$. For the case with a wavenumber cutoff at $|\boldsymbol{k}|/k_p = 2.4$, augmented kurtosis is accompanied by comparatively more aggressive spectral changes including redevelopment of the spectral tail. Similar trends are observed for the case with a wavenumber cutoff at $|\boldsymbol{k}|/k_p = 6$, but the spectral changes are less substantial. Thus, the spectral tail appears to play an important role in a form of spectral equilibrium that reduces spectral changes and decreases the peak kurtosis value. Our findings suggest that care should be taken when truncating the spectral tail for the purpose of simulations/experiments. We also find that the equation of Fedele (2015, "On the Kurtosis of Deep-Water Gravity Waves," J. Fluid Mech., 782, pp. 25–36) provides an excellent estimate of the peak kurtosis value. However, the bandwidth parameter must account for the spectral tail to provide accurate estimates of the peak kurtosis. [DOI: 10.1115/1.4055480]

Keywords: hydrodynamics, ocean waves and associated statistics

1 Introduction

Rogue wave occurrence in random seas and the evolution of free-surface kurtosis remain active areas of research. Dispersive focusing based on wave components with different frequencies and directions can result in the formation of extreme waves (see, for example, Fedele et al. [1]). Nonlinear interactions between wave components can also alter the dispersive characteristics of a wave field, allowing for self-focusing (Janssen [2]). The relative importance of nonlinear interactions in the formation of rogue waves has been a focus of previous studies with comprehensive reviews [3–6].

In the context of random seas, a deviation from Gaussian statistics indicates the presence of nonlinear interactions. The kurtosis of the free surface, $\mathrm{Kur} = \langle \eta^4 \rangle / \langle \eta^2 \rangle^2$, has received particular attention, as an indicator of nonlinear interactions and rogue wave occurrence (see, e.g., Mori and Janssen [7]). Here, η denotes the free-surface elevation and the angled brackets denote a statistical average. The *excess kurtosis*, denoted as C_4, quantifies the deviation from Gaussian statistics:

$$C_4 = \frac{\langle \eta^4 \rangle}{3\langle \eta^2 \rangle^2} - 1 \tag{1}$$

yielding $C_4 = 0$ for a Gaussian process, associated with linear seas. The excess kurtosis C_4 is comprised of dynamic (C_4^d) and bound (C_4^b) contributions such that $C_4 = C_4^d + C_4^b$, where the dynamic contribution accounts for the buildup of phase correlation and the bound contribution accounts for the presence of bound harmonics (see, e.g., Refs. [8,9] for a more detailed discussion on bound harmonics). Dynamics excess kurtosis values of $C_4^d > 0$ and $C_4^d < 0$ are, respectively, indicative of focusing and defocusing due to nonlinear interactions.

An analytical solution for dynamic kurtosis (C_4^d) has been presented by Fedele [10], based on narrow-band directional waves with a Gaussian-type spectrum. The initial condition is based on Gaussian statistics, $C_4^d(t_0) = 0$, with random component phases and amplitudes. Fedele [10] assumes that the wave field is spatially homogeneous and nonstationary in time. The analysis of this problem originates from Janssen [2], providing an expression for the dynamic excess kurtosis of weakly nonlinear unidirectional seas. Reference [7] extended the work of Ref. [2] based on the assumption of narrow-bandedness. References [11,12] considered the role of directional effects. Fedele [10] provides an expression for dynamic kurtosis in the directional case, based on:

$$\frac{\mathrm{d}C_4^d(\tau)}{\mathrm{d}\tau} = \mathrm{BFI}^2 \frac{\mathrm{d}J}{\mathrm{d}\tau} \tag{2}$$

Here, τ represents nondimensional time, $\tau = \nu^2 \omega_0 t$, where ν is the spectral width and $\omega_0 = 2\pi/T_0$ is the characteristic frequency based on the characteristic wave period T_0. The Benjamin–Feir index (BFI) is given by:

$$\mathrm{BFI} = \frac{\mu\sqrt{2}}{\nu} \tag{3}$$

based on the wave steepness $\mu = k_0\sigma$, where k_0 is the characteristic wavenumber and σ is the standard deviation of the free surface, $\sigma^2 = \langle \eta^2 \rangle$. Note that the definition in Eq. (3) is a factor of $\sqrt{2}$ smaller than the one used in some other studies, e.g., Onorato et al. [13]. The function $J(\tau, R)$ in (2) depends on the short-crestedness parameter R:

$$R = \frac{1}{2}\frac{\sigma_\theta^2}{\nu^2} \tag{4}$$

[1]Corresponding author.

Contributed by the Ocean, Offshore, and Arctic Engineering Division of ASME for publication in the Journal of Offshore Mechanics and Arctic Engineering. Manuscript received March 25, 2022; final manuscript received August 26, 2022; published online October 3, 2022. Assoc. Editor: Nilanjan Saha.

Here, σ_θ is the angular width of the spectrum, which quantifies the directional spreading of the waves. Fedele [10] calculates the angular width σ_θ based on the spreading function of the spectrum, $D(\theta)$:

$$\sigma_\theta = \sqrt{\frac{\int_0^{\pi/2} \theta^2 D(\theta) \mathrm{d}\theta}{\int_0^{\pi/2} D(\theta) \mathrm{d}\theta}} \tag{5}$$

by using the short-crestedness parameter R and nondimensional time τ, Fedele [10] found the expression:

$$\frac{\mathrm{d}J}{\mathrm{d}\tau} = 2\mathrm{Im}\left(\frac{1}{\sqrt{1 - 2i\tau + 3\tau^2}\sqrt{1 + 2iR\tau + 3R^2\tau^2}}\right) \tag{6}$$

required to evaluate (2). Here, $\mathrm{Im}(x)$ denotes the imaginary part of x. Figure 1 shows the evolution in kurtosis predicted for a range of R values. As can be seen, the peak kurtosis value is significantly impacted by the value of R, suggesting a strong dependency on the bandwidth and spreading of the waves, as well as the steepness.

Previous studies have investigated the evolution of kurtosis for random seas, including the experiments of Onorato et al. [13] as well as the higher-order spectral (HOS) and modified nonlinear Schrödinger (MNLS) simulations of Toffoli et al. [14] and Xiao et al. [15]. In this study, we perform random seas simulations using the MNLS equation of Trulsen et al. [16] based on an exact linear dispersion operator. Our simulations are based on the sea-state parameters used in Experiment B of Onorato et al. [13], a case also considered by Toffoli et al. [14] and Xiao et al. [15]. Thus, we compare our results with those of previous studies. We note that the experiments of Onorato et al. [13] are based on wave fields, which are inhomogeneous in space but stationary in time for a given location. In contrast, our simulations are based on a spatially homogeneous random sea, which is nonstationary in time, as simulated by Xiao et al. [15] and Toffoli et al. [14]. However, for narrow-banded seas with low directional spreading, mapping between space and time can be performed with the group velocity, although we note this is an extra approximation. Toffoli et al. [14] performed MNLS simulations of both types (spatially homogeneous and nonstationary as well as spatially inhomogenous and stationary) and found that the kurtosis curves agreed well for the narrow-banded case considered in this study. Thus, we use the experimental results of Onorato et al. [13] in our comparisons. Our investigation focuses on the impact of the spectral tail on kurtosis evolution, exploring the role of the tail in establishing a form spectral equilibrium that reduces the peak kurtosis.

The concept of spectral equilibrium has been considered by previous studies. Nonequilibrium sea states are characterized by comparatively rapid spectral changes that eventually slow down as the sea state moves toward a better representation of equilibrium for the given conditions. As discussed in Ref. [17], wave–current interactions, sudden changes in bathymetry, and meteorological conditions are all possible causes of nonequilibrium, provoking the occurrence of rapid spectral changes (see, e.g., Refs. [18–20]). The investigation of Barratt et al. [21] showed that steep wave groups formed under nonequilibrium conditions may exhibit augmented kinematics and a prolonged lifespan—the presence of a fully developed spectral tail was found to reduce the nonlinear features of the wave groups. Physical mechanisms that may impact the development of the spectral tail have also been identified by previous studies. Background currents have been shown to possibly suppress the development of the spectral tail [22]. Ice sheets also tend to dissipate the energy associated with high-wavenumber components in the spectral tail [23,24]. Simulations based on initial spectra that do not include a fully developed tail also tend to exhibit rapid spectral evolution in the early stages (see, e.g., Res. [15,25]). Our simulations are focused on the impact of the spectral tail on the evolution of random seas initialized with Gaussian statistics.

As discussed earlier, it is possible for the wave spectrum to be curtailed in nature. However, a more common engineering issue is where the spectrum is curtailed in a laboratory setting due to bandwidth limitations of wavemakers. If waves are made in the lab, which do not reflect the reality in the ocean, this needs to be understood as otherwise we will incorrectly estimate loads on offshore structures from model tests.

To help understand, this perform simulations based on JONSWAP spectra truncated at different wavenumbers to alter the bandwidth and prominence of the spectral tail. We monitor the consequent kurtosis evolution and explain the trends based on the spectral evolution we observe. Finally, we calculate approximate R values and compare our results to Eq. (2) to assess the extent of the agreement.

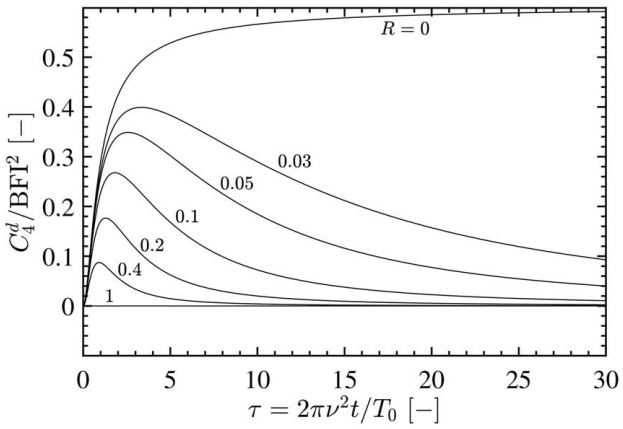

Fig. 1 Dynamic excess kurtosis normalized by the square of the Benjamin–Feir index (C_d^4/BFI^2) as a function of nondimensional time ($\tau = \nu^2\omega_0 t$) for different values of R, based on Fedele [10]

2 Numerical Details

We perform random-sea MNLS simulations based on Rayleigh distributed component amplitudes with a uniform phase distribution. We consider two distinct cases, each with a different cutoff wavenumber for the spectral tail. Each case has been simulated a total of 20 times with a new random seed generated for each instance. Our analysis of the spectral evolution is based on ensemble averaging of the resultant spectra over the following 150 wave periods.

2.1 Initial Conditions. We define the variance density spectrum $S(\omega, \theta)$ as the product of a frequency spectrum $F(\omega)$ and a spreading function $D(\theta)$, where ω represents the angular frequency and θ represents the direction of the wave component:

$$F(\omega, \theta) = S(\omega)D(\theta) \tag{7}$$

Following Onorato et al. [13], we use the JONSWAP formulation as the frequency spectrum:

$$F(\omega) = \frac{\alpha g^2}{\omega^5} \exp\left[-\frac{5}{4}\left(\frac{\omega}{\omega_p}\right)^{-4}\right] \gamma^{\exp[-(\omega-\omega_p)^2/(2\sigma^2\omega_p^2)]} \tag{8}$$

where ω is the angular frequency and ω_p is the peak frequency, α is the Phillips parameter, γ is the peak enhancement factor, and the parameter σ is frequency dependent: $\sigma = 0.07$ for $\omega \le \omega_p$ and $\sigma = 0.09$ for $\omega > \omega_p$. We use the cosine-squared spreading function:

$$D(\theta) = \begin{cases} \frac{2}{\Theta}\cos^2\left(\frac{\pi\theta}{\Theta}\right) & \text{for } |\theta| \le \Theta/2 \\ 0 & \text{for } |\theta| > \Theta/2 \end{cases} \tag{9}$$

where θ is the wave propagation direction and Θ is the directional spreading width of the cosine-squared function. We note the

Table 1 Sea-state parameters

γ	ω_p	k_p	Θ	H_s	ε
6.0	0.5257 s^{-1}	0.02796 m^{-1}	12 deg	11.2 m	0.16

relationship between σ_θ in (5) and Θ in (9), given by:

$$\sigma_\theta = \Theta\sqrt{\frac{\pi^2 - 6}{12\pi^2}} \tag{10}$$

The products of (8) and (9) yield the variance density spectrum in the (ω, θ) coordinate system. The corresponding wavenumber spectrum in (k_x, k_y) can be calculated with the Jacobian: $\hat{S}(k_x, ky) = (1/k)(\mathrm{d}\omega/\mathrm{d}k)S(\omega, \theta) = (g^2/(2\omega^3))S(\omega, \theta)$, where $\boldsymbol{k}$ is the wavenumber vector $\boldsymbol{k} = (k_x, k_y)$, and we have used the deep-water dispersion relationship.

To perform random-sea simulations, we require Rayleigh distributed component amplitudes, a_i, with expected values, μ_i, that are consistent with the defined wavenumber spectrum, $\hat{S}(\boldsymbol{k})$. The expected amplitude for component $\boldsymbol{k}_i$ follows from the wavenumber spectrum:

$$\mu_i = \sqrt{2\hat{S}(\boldsymbol{k}_i)} \tag{11}$$

Thus, the scale parameter of the Rayleigh distribution is given by $\sqrt{2/\pi}\,\mu_i$, and we generate the random amplitude, a_i, for component $\boldsymbol{k}_i$ using:

$$a_i = \sqrt{2/\pi}\;\mu_i\sqrt{-2\ln\chi} \tag{12}$$

where χ is a uniformly distributed random variable within the range [0, 1] and ln is the natural logarithm. A random phase offset φ_i is also generated for each wavenumber component $\boldsymbol{k}_i$ in the range $[0, 2\pi]$. We compute the linear surface elevation at each point in space $\boldsymbol{x} = (x, y)$ as a superposition of the components:

$$\eta_L(\boldsymbol{x}, t) = \sum_i a_i \cos(\boldsymbol{k}_i \cdot \boldsymbol{x} - \omega_i t + \varphi_i) \tag{13}$$

using the deep-water linear dispersion relationship $\omega_i = \sqrt{g|\boldsymbol{k}_i|}$ to calculate the component frequencies. For the MNLS simulations, we calculate the initial complex envelope $B(\boldsymbol{x}, t_0)$ using the linear surface elevation η_L and the corresponding Hilbert transform η_L^H [26]:

$$B(\boldsymbol{x}, t_0) = \{\eta_L + i\eta_L^H\}\exp(-i[\boldsymbol{k}_0 \cdot \boldsymbol{x} - \omega_0 t_0]) \tag{14}$$

where $\boldsymbol{k}_0$ and ω_0 represent the characteristic wavenumber and frequency of the carrier wave.

The parameters used in this study are listed in Table 1. We use a peak enhancement factor (γ) of 6.0. The spectral peak of the JONSWAP, in terms of angular frequency (ω_p) and wavenumber (k_p), are both listed in Table 1 (note that ω_p and k_p are not simply related by the linear dispersion relation due to the presence of a Jacobian). The characteristic time and length scales associated with k_p are also listed in Table 3. We use a directional spreading width (Θ) of 12 deg, based on the spreading function defined in Eq. (9), the same value as mentioned in Ref. [15]. Our significant wave height (H_s) of 11.2 m corresponds to a wave steepness ($\varepsilon = k_p H_s/2$) of 0.16. As calculated by Fedele [10], the parameters listed in Table 1 correspond to a BFI ($=\mu\sqrt{2}/\nu$) of 0.78, where $\mu = \varepsilon/2$ and ν is a measure of spectral bandwidth.

We use an exponential low-pass filter to truncate the tail of the spectrum following [15]:

$$\Omega(|\boldsymbol{k}|/k_p, \beta_1, \beta_2) = \exp\left(-\left[\frac{|\boldsymbol{k}|}{\beta_1 k_p}\right]^{\beta_2}\right) \tag{15}$$

Table 2 Low-pass filter parameters for spectral tail truncation

Case	β_1	β_2	Cutoff wavenumber
ST	2.4	20	$\lvert\boldsymbol{k}\rvert/k_p = 2.4$
LT	6	35	$\lvert\boldsymbol{k}\rvert/k_p = 6$

Table 3 Discretization parameters

Characteristic scales	Wavelength (λ_0) 225 m Wave period (T_0) 12.0 s
Numerical domain	Length (L) 30.72 km Width (W) 20.48 km
Discretization	$N_x = 2049$, $\Delta x = 15$ m $N_y = 1025$, $\Delta y = 20$ m $N_t = 4501$, $\Delta t = 0.4$ s

We consider two test cases labeled case ST and case LT, where "ST" refers to a short tail and "LT" refers to a long tail for the spectrum. β_1 and β_2 values are listed in Table 2 together with the corresponding cutoff wavenumbers. Case ST and LT feature truncation of the spectral tail at approximately $|\boldsymbol{k}|/k_p = 2.4$ and $|\boldsymbol{k}|/k_p = 6$, respectively, based on the β_1 and β_2 listed in Table 2. The resultant initial conditions are shown in Fig. 3(*a*) for case ST and Fig. 4(*a*) for case LT. We note that approximately 21% of the total energy for case LT is associated with wavenumber components with $|\boldsymbol{k}|/k_p > 2.4$.

2.2 MNLS Simulations. We perform our random-sea simulations using the MNLS equation of Trulsen et al. [16], a modified version of the Trulsen and Dysthe [27] equation:

$$\frac{\partial B}{\partial t} + \mathfrak{Q}\,B + \frac{1}{2}i\omega_0 k_0^2|B|^2 B + \frac{3}{2}\omega_0 k_0|B|^2\frac{\partial B}{\partial x} + \frac{1}{4}\omega_0 k_0 B^2\frac{\partial B^*}{\partial x} + ik_0\frac{\partial\overline{\phi}}{\partial x}B = 0 \tag{16}$$

Here, B^* denotes the conjugate of the complex envelope and $\overline{\phi}$ denotes the mean flow potential. The carrier wave is aligned with the x-axis, $\boldsymbol{k}_0 = (k_0, 0)$, so that k_0 in (16) represents the carrier wavenumber, and the characteristic frequency ω_0 is related to the carrier wavenumber k_0 by the deep-water linear dispersion relationship, $\omega_0 = \sqrt{gk_0}$. The dispersion operator $\mathfrak{Q}$ in (16) is based on a pseudo-differential operator that preserves the exact linear dispersion relationship, as explained by Trulsen et al. [16]:

$$\mathfrak{Q}\,B = \frac{1}{4\pi^2}\int_{-\infty}^{\infty} i[\omega(\boldsymbol{k_0} + \boldsymbol{\mu}) - \omega_0]\exp(i\boldsymbol{\mu}\cdot(\boldsymbol{x} - \boldsymbol{y}))B(\boldsymbol{y}, t)\mathrm{d}\boldsymbol{y}\mathrm{d}\boldsymbol{\mu} \tag{17}$$

Here, $\boldsymbol{\mu} = (\lambda, \mu)$ is the modulation wavenumber. Direct numerical evaluation of Ref. (17) avoids expansion and truncation of the linear dispersion relation, increasing the bandwidth limits of the MNLS equation and improving the resolution of four-wave interactions while reducing energy leakage (see Refs. [28] and [29] for a discussion on MNLS energy leakage), with almost no additional computational cost. Barratt and Adcock [30], building on Refs. [31,32], performed a detailed comparison of the exact and truncated versions of the dispersion operator for focused wave groups. The MNLS equation in (17) is subject to free surface and bottom boundary conditions, as well as continuity for the mean flow potential $\overline{\phi}$:

$$\frac{\partial\overline{\phi}}{\partial z} = \frac{\omega_0}{2}\frac{\partial}{\partial x}|B|^2 \quad \text{at } z = 0 \tag{18}$$

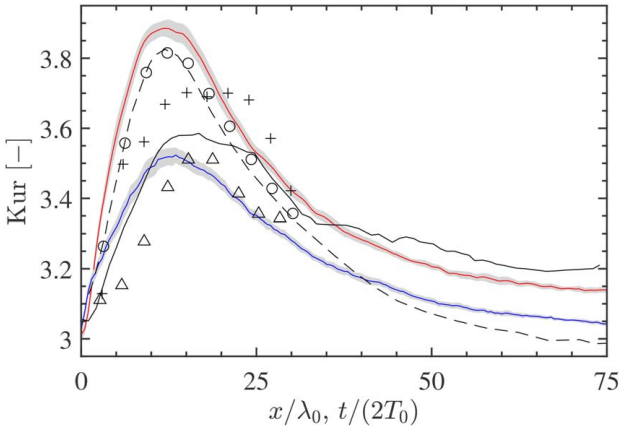

Fig. 2 Kurtosis evolution for case ST (red/higher line with error bar) and Case LT (blue/lower line with error bar) compared against other studies, including (△) the experiments of Onorato et al. [13]. The shaded gray bands represent 95% confidence intervals. The simulation results of Xiao et al. [15] are shown: (– – –) MNLS and (——) HOS as well as the simulation results of Toffoli et al. [14]: (◯) MNLS and (+) HOS. All the results are based on JONSWAP spectra ($\gamma = 6$) with steepness $\varepsilon = 0.16$ and a Benjamin–Feir index (BFI) of 0.78 based on the definition in Eq. (3).

$$\frac{\partial \overline{\phi}}{\partial z} = 0 \quad \text{at } z = -\infty \tag{19}$$

$$\nabla^2 \overline{\phi} = 0 \quad \text{for } -\infty < z < 0 \tag{20}$$

We incorporate the boundary conditions (18) and (19), directly into the MNLS equation (16), using the continuity condition for the mean flow (20), as done with the fourth-order envelope equation of Janssen [33]. A single governing equation is, thus, obtained:

$$\frac{\partial B}{\partial t} + \mathfrak{L}\, B + \frac{1}{2} i\omega_0 k_0^2 |B|^2 B + \frac{3}{2}\omega_0 k_0 |B|^2 \frac{\partial B}{\partial x} + \frac{1}{4}\omega_0 k_0 B^2 \frac{\partial B^*}{\partial x} + ik_0 B \mathcal{F}^{-1}\left\{ \frac{ik_x}{|\boldsymbol{k}|} \mathcal{F}\left\{ \frac{\omega_0}{2} \frac{\partial}{\partial x} |B|^2 \right\} \right\} = 0 \tag{21}$$

where $\mathcal{F}$ denotes a 2D Fourier transform in x and y and $\mathcal{F}^{-1}$ denotes the inverse operation. The expression in (21) is based on the evaluation of the bottom boundary condition (19) at $z = -\infty$ and is, therefore, a deep-water equation. Thus, we obtain the initial complex envelope using (14), and the envelope is marched forward in time with (21). We discretize and numerically solve Eq. (21) using a split-step algorithm. We use spectral methods to evaluate the linear dispersion operator $\mathfrak{L}B$ in (17), and we use fourth-order finite differencing with symmetric stencils for the spatial derivatives in the nonlinear terms. Time marching is performed with the classic fourth-order Runge-Kutta scheme. The details of the discretization are listed in Table 3, including the length (L) and width (W) of the domain. The number of grid points in the x direction and y direction are listed, denoted as N_x and N_y respectively, together with the corresponding grid spacings, Δx and Δy. The size of the domain ensures 136 characteristic wavelengths (λ_0) in the x-direction and $91\lambda_0$ in the y direction, where $\lambda_0 = 2\pi/k_0$. The characteristic length scales of the wave envelope can be approximated with:

$$\Lambda_x = \frac{2\pi}{k_w}, \qquad \Lambda_y = \frac{2\pi}{k_0 \sigma_\theta} \tag{22}$$

based on the characteristic length scales for the wavenumber (k_0), bandwidth (k_w), and spreading parameter (ς_0). Dimensionless metrics for grid resolution, in the x and y directions can, thus, be defined as follows:

$$n_x = \frac{\Lambda_x}{\Delta x}, \quad n_y = \frac{\Lambda_y}{\Delta y} \tag{23}$$

which approximately represent the number of grid points spanning the length scale of the wave envelope in the x and y directions. On the basis of the initial conditions, we use the peak of the wavenumber spectrum, $k_0 = 0.02796\ \text{m}^{-1}$, and we use Eq. (5) to obtain $\sigma_\theta = 0.04$ rad. We estimate the bandwidth k_w for case ST and case LT using the spectral half-width and obtain $k_w = 0.004\ \text{m}^{-1}$. Combined with the grid resolution listed in Table 3, we obtain $n_x \approx 105$ and $n_y \approx 281$. The simulations are time marched for a total of 150 wave periods (T_0), where $T_0 = 2\pi/\omega_0$, with a timestep (Δt) of 0.4 s. By using the group velocity of the wave envelope as the characteristic velocity, we calculate a Courant–Friedrichs–Lewy condition of 0.25 for our MNLS simulations, based on the discretization parameters listed in Table 3. To assess the diffusivity of our simulations, we have considered the conserved quantity I_2 [34]:

$$I_2 = \sum_{i,j} |B(x_i, y_j)|^2 \tag{24}$$

typically associated with energy conservation. We found the quantity I_2 to be conserved within 1% of the initial value over the entire duration of all our simulations, indicating permissibly low levels of diffusivity. We find that the $|B|^2\, \partial B/\partial x$ term in (16) is particularly prone to causing simulation divergence. Thus, we apply spectral filtering to eliminate high-frequency contributions from this term—we set all components above $|\boldsymbol{k}|/k_p = 5$ to zero when calculating $|B|^2\, \partial B/\partial x$.

2.3 Spectral Parameters. We analyze the spectral evolution of case ST and Case LT using statistical parameters to characterize the spectral peak, bandwidth, and directional spreading. Our selection of the spectral parameters is largely based on the review by Serio et al. [35]. For each simulation, we perform a two-dimensional discrete Fourier transform (in x and y) on the surface elevation once per wave period and use the result to calculate the

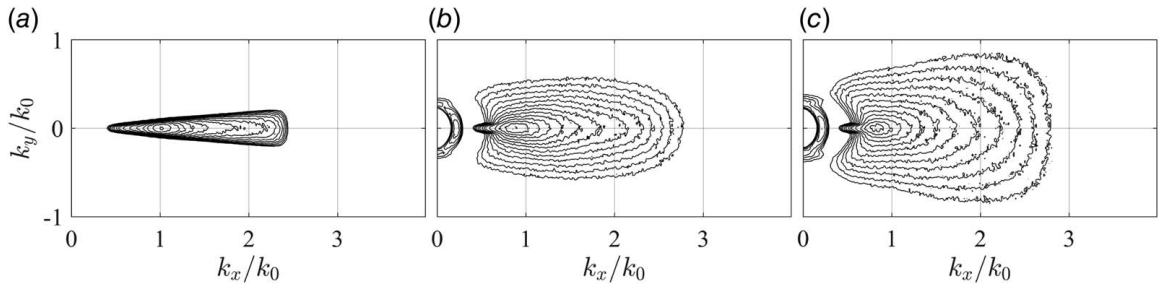

Fig. 3 Contour plots of the ensemble-averaged variance density spectrum $\overline{S}(k_x, k_y)$ for case ST featuring truncation of the spectral tail in the vicinity of $|\boldsymbol{k}|/k_p = 2.4$: (a) $t/T_0 = 0$, (b) $t/T_0 = 50$, and (c) $t/T_0 = 100$. The contour levels are logarithmic, ranging from 1×10^{-5} to 1×10^{-2}.

variance density spectrum in terms of wavenumber $S(k_x, k_y, t)$ based on a Cartesian coordinate system:

$$S(k_x, k_y, t) = \frac{1}{2}|\hat{\eta}(k_x, k_y, t)|^2 \tag{25}$$

where $\hat{\eta}$ represents the Fourier components of the surface elevation. Arithmetic averaging over the ensemble ($N_i = 20$) at time t yields the ensemble-averaged spectrum $\overline{S}(k_x, k_y, t)$:

$$\overline{S}(k_x, k_y, t) = \frac{1}{N_i}\sum_{i}^{N_i} S_i(k_x, k_y, t) \tag{26}$$

Converting to a polar coordinate system with the use of a Jacobian, $\overline{S}(k, \theta, t) = k\overline{S}(k_x, k_y, t)$, we characterize the directional spreading of the ensemble-averaged variance density spectrum:

$$\varsigma(t) = \sqrt{\frac{\sum_j \theta_j^2\ \overline{S}(k_j, \theta_j, t)}{\sum_j \overline{S}(k_j, \theta_j, t)}} \tag{27}$$

Here, k represents the magnitude of the component wavenumber $|\boldsymbol{k}|$ for convenience of notation. To characterize the spectral peak and the bandwidth, we calculate the frequency spectrum $\overline{S}(f, \theta, t) = J\ \overline{S}(k, \theta, t)$, where $J = 4\pi\sqrt{k/g}$. Integration over θ yields the omnidirectional frequency spectrum $\overline{S}(f, t)$ used to estimate the peak frequency:

$$f_p(t) = \frac{\sum_j f_j[\overline{S}(f_j, t)]^4}{\sum_j [\overline{S}(f_j, t)]^4} \tag{28}$$

based on the omnidirectional frequency spectrum raised to the fourth power, as recommended by Young [36]. We also estimate the bandwidth based on the omnidirectional frequency spectrum, using the peakedness parameter introduced by Goda [37]:

$$Q_p(t) = \frac{2}{m_0^2}\int_0^\infty f[\overline{S}(f, t)]^2 \mathrm{d}f \tag{29}$$

where

$$m_0 = \int_0^\infty \overline{S}(f, t_0)\mathrm{d}f \tag{30}$$

We use the trapezoidal method to perform the numerical integration in Eq. (29) based on unequal point spacing. Our estimate of spectral bandwidth (ν) relates inversely to the peakedness parameter Q_p:

$$\nu(t) = \frac{1}{\sqrt{\pi}\, Q_p} \tag{31}$$

consistent with the bandwidth metric used by Serio et al. [35] to calculate the Benjamin–Feir index (BFI). We also use ν in (31) as our bandwidth metric when calculating the BFI. The spectral parameters defined in Eqs. (27), (28), and (31) thus form the basis of our spectral evolution analysis.

3 Results and Discussion

We analyze the kurtosis evolution for case ST and case LT and explain the observations based on the spectral evolution, using contour plots of the ensemble-averaged spectra as well as the parameters defined in Eqs. (27), (28), and (31). Finally, we compare the simulation results for kurtosis with the theory of Fedele [10], and we briefly discuss the selection of an appropriate bandwidth parameter to characterize each case.

3.1 Kurtosis Evolution. The evolution of kurtosis for our MNLS simulations is shown in Fig. 2, including both dynamic and bound contributions up to the third order. The shaded gray bands represent 95% confidence intervals for the ensemble-averaged MNLS results. The experimental results of Onorato et al. [13] are also shown. Both Toffoli et al. [14] and Xiao et al. [15] performed similar simulations to those in this study, using the MNLS equation as well as a HOS code, and the results are depicted in Fig. 2. As discussed in Sec. 1, the results of Onorato et al. [13] are based on waves propagating along a tank. We perform space/time mapping with the group velocity for the purposes of comparing our simulation results to the experiments of Onorato et al. [13]. The x-axis in Fig. 2 shows the corresponding spatial x/λ_0 or temporal $t/(2T_0)$ parameter with kurtosis shown on the y-axis (excluding the contribution of bound harmonics). Here, λ_0 and T_0 represent the characteristic wavelength and wave period, respectively. We see good agreement between the MNLS simulations results of Toffoli et al. [14], Xiao et al. [15], and case ST of this study. A peak kurtosis value of 3.89 is observed for case ST, and agreement between the MNLS simulations appears to be particularly good in the vicinity of the peak. Similar to case ST of this study, the MNLS simulations of both Toffoli et al. [14] and Xiao et al. [15] effectively truncated the wavenumber spectrum of the surface elevation at $|\boldsymbol{k}|/k_p = 2$, by limiting the modulation wavenumber of the envelope to $|\boldsymbol{\mu}|/k_p \leq 1$. Here, $\boldsymbol{\mu} = (\lambda, \mu)$ is the modulation wavenumber defined relative to the wavenumber of the carrier wave, $\boldsymbol{k} = (k_p, 0)$. Thus, Fig. 2 also serves to verify our simulations. The HOS results of Toffoli et al. [14] and Xiao et al. [15] differ, however, from the MNLS results for case ST and agree better with the MNLS results for case LT as well as the experimental results of Onorato et al. [13]. Case LT is based upon a spectral tail truncated at $|\boldsymbol{k}|/k_p = 6$ and, thus, features a more prominent spectral tail. Likewise, the experiments of Onorato et al. [13] and the HOS simulations of Toffoli et al. [14] and Xiao et al. [15] all included a fully developed spectral tail in the initial conditions. Thus, the differences between case ST and case LT appear to be the result of the spectral tail, and the findings are consistent other studies. Case LT, in this study, reaches a peak kurtosis value of 3.52, approximately 10% lower than the peak kurtosis value for case ST. Inclusion of the spectral tail up to $|\boldsymbol{k}|/k_p = 6$ in the initial conditions, thus, appears to reduce the peak kurtosis value, while artificial truncation of the spectral tail at $|\boldsymbol{k}|/k_p = 2.4$ augments the peak kurtosis value. The relatively good agreement between case LT and the experiments/HOS results also suggests

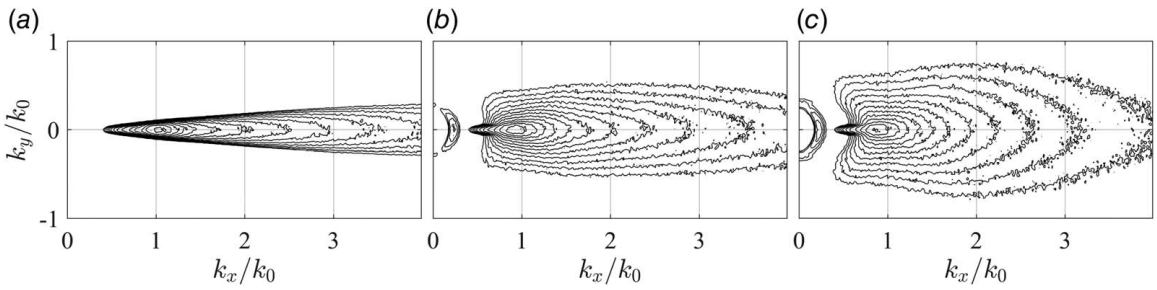

Fig. 4 Contour plots of the ensemble-averaged variance density spectrum $\overline{S}(k_x, k_y)$ for case LT featuring truncation of the spectral tail in the vicinity of $|\boldsymbol{k}|/k_p = 6$: (a) $t/T_0 = 0$, (b) $t/T_0 = 50$, and (c) $t/T_0 = 100$. The contour levels are logarithmic, ranging from 1×10^{-5} to 1×10^{-2}.

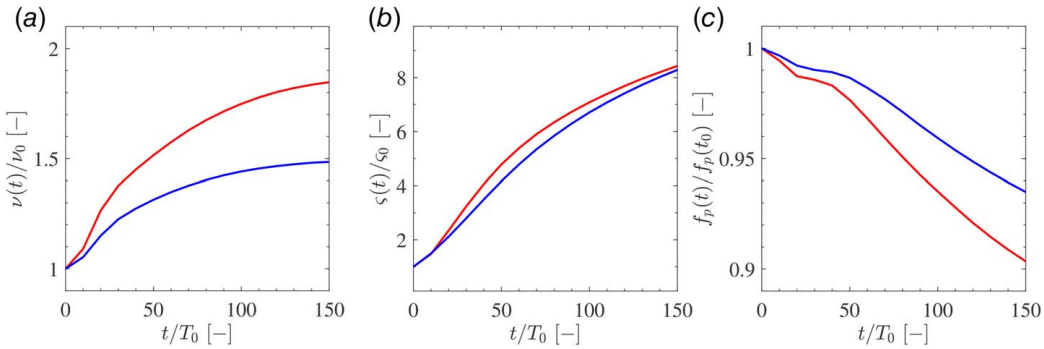

Fig. 5 Evolution of ensemble-averaged spectral parameters for case ST (red line (higher in (*a*,*b*), lower in (*c*)) and case LT (blue line (lower in (*a*,*b*), higher in (*c*)): (*a*) spectral bandwidth ν defined in (31), (*b*) spreading parameter ς defined in (27), and (*c*) peak frequency f_p defined in (28)

that the MNLS equation provides better kurtosis estimates if the spectral tail is included, despite the narrow-bandwidth limitations of the equation.

3.2 Spectral Evolution. To clarify the trends in kurtosis observed in the previous section, we have analyzed the evolution of the ensemble-averaged variance density spectrum, $\overline{S}(k_x, k_y)$, for case ST and case LT with the results shown in Figs. 3 and 4, respectively. The wavenumbers k_x and k_y have been normalized by the characteristic wavenumber $k_0 = 0.02796\ \mathrm{m}^{-1}$, the initial spectral peak listed in Table 1. The contour plots in each figure are shown at times: (a) $t/T_0 = 0$; (b) $t/T_0 = 50$; and (c) $t/T_0 = 100$. Note that the contour levels are logarithmically distributed. As shown in Fig. 3(*a*), case ST features a narrow-banded spectrum with truncation of the tail in the vicinity of $|\boldsymbol{k}|/k_p = 2.4$. Figures 3(*b*) and 3(*c*) reveal the rapid broadening of the spectrum, which occurs during the simulation—the truncated tail partially redevelops and the directional spreading increases. Similar features are apparent for case LT, shown in Fig. 4. Case LT features a more prominent spectral tail for the initial conditions since truncation is performed in the vicinity of $|\boldsymbol{k}|/k_p = 6$. However, rapid broadening of the spectrum over time is also observed for case LT, although less directional spreading is apparent in Figs. 4(*b*) and 4(*c*) than the corresponding plots in Fig. 3. The differences in spectral evolution between case ST and case LT are best captured by the statistical parameters defined in (27), (28), and (31).

Figure 5 shows the evolution of the ensemble-averaged spectral parameters for case ST and case LT. The spectral bandwidth parameter ν, defined in (31), is shown in Fig. 5(*a*). The spreading parameter ς, defined in (27), is shown in Fig. 5(*b*). The peak frequency f_p, defined in (28), is shown in Fig. 5(*c*). All of the parameters have been normalized by their initial value, at time t_0. Figure 5(*a*) shows that both case ST and case LT exhibit an increase in spectral bandwidth; however, the increase in ν/ν_0 is more rapid for case ST and the final value of 1.85 exceeds the final value of 1.48 for case LT by approximately 25%. Similarly, the spreading parameter in Fig. 5(*b*) also exhibits an increase in ς/ς_0 for both cases—the values are similar toward the start and end of the simulations; however, case ST exhibits a more rapid increase in between. Finally, Fig. 5(*c*) demonstrates a reduction in the peak frequency for both cases, consistent with the downshift of the spectral peak observed in other studies (see, e.g., [36,37]). The frequency downshift is also observed to occur more rapidly for case ST than case LT, and the final value of 0.903 for case ST is approximately 4% lower than the final value of 0.935 observed for case LT. Thus, all the spectral parameters indicate that the spectral changes for case ST occur more rapidly and are more pronounced than those of case LT. Inclusion of a more prominent spectral tail in case LT thus appears to reduces the spectral changes observed during the simulations. Truncation of the spectral tail close to the spectral peak in case ST conversely augments the spectral changes, which occur during the simulations. Thus, the spectral tail appears to play an important role in establishing the spectral equilibrium of the sea state and care should be taken when truncating the tail in a simulation or laboratory setting. The kurtosis results shown in Fig. 2 indicate that the rapid spectral changes in case ST augment the peak kurtosis value, relative to case LT, demonstrating the importance of the tail in determining the peak kurtosis.

3.3 Comparison With Theory. We compare our ensemble-averaged kurtosis results with the solution of Fedele [10], with the results shown in Fig. 6. The kurtosis curves for both cases ST and LT are shown, expressed as dynamic excess kurtosis, see (1), normalized by the square of the Benjamin–Feir index, see (3). The kurtosis curves have been plotted against nondimensional time, $\tau = \nu^2\omega_0 t$, based on the spectral bandwidth (ν) and the characteristic frequency (ω_0). Our calculation of the shortcrestedness parameter R is based on (4) using the angular width in (5). The dashed line in Fig. 6, calculated by Fedele [10], bases the bandwidth parameter ν on the spectral half-width and, thus yields $R = 0.032$ with the same curve for case ST and case LT (since the spectral half-width is not altered by truncation of the tail). The solid ($R = 0.022$) and dotted ($R = 0.052$) lines in Fig. 6 are based on the bandwidth parameter in (31), which does account for truncation of the spectral tail. As can be seen, the kurtosis curves based on (31) provide better agreement with the simulation results, compared with the curve based on the spectral half-width.

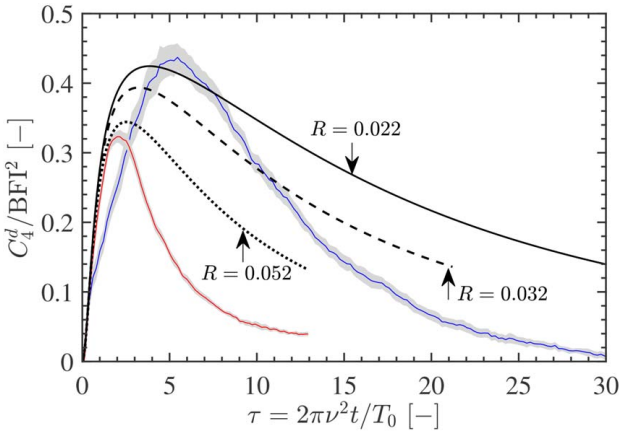

Fig. 6 Kurtosis evolution for case ST (red line (peaks earlier and lower)) and case LT (blue line (peaks later and higher)) compared against the solution of Fedele [10] based on different bandwidth parameters: (dashed, − − −) bandwidth based on spectral half-width for both case ST and case LT yields $R = 0.031$; (dotted, ··· ···) bandwidth based on (31) for case ST yields $R = 0.052$; (solid, ——) bandwidth based on (31) for case LT yields $R = 0.022$. The shaded gray bands represent 95% confidence intervals for the ensemble-averaged results.

We note that the peak kurtosis value is particularly well predicted, although the long-term behavior differs—the kurtosis decline after the peak occurs faster for the simulations than predicted by the theoretical results. Thus, we find that Fedele [10] provides an excellent estimate for the peak kurtosis value in our simulations. However, the bandwidth parameter ν must account for the spectral tail to accurately predict the kurtosis peak. We find that the bandwidth parameter in (31), based on the peakedness parameter of Goda [37], appears to be suitable for this purpose, consistent with the recommendations of Serio et al. [35].

4 Conclusion

Our findings indicate that artificial truncation of the spectral tail augments the peak kurtosis value of a random sea initialized with Gaussian statistics. Truncation of the tail results in more aggressive spectral changes during the simulation, characterized by spectral broadening in terms of bandwidth and spreading as well as downshifting of the spectral peak as shown in Fig. 6. The spectral tail is also observed to redevelop during the course of the simulation. Thus, the spectral tail appears to play an important role in establishing a form of spectral equilibrium that reduces spectral changes and decreases the peak kurtosis value. We find that the MNLS equation of Trulsen et al. [16] can be used to estimate the peak kurtosis value, by including the spectral tail in the initial conditions, despite the bandwidth limits of the equation.

This article strongly indicates that suppression of the high-frequency components can lead to an increase number of large waves. This is of most practical importance in the laboratory. In many laboratory experiments, we wish to replicate open ocean conditions. However, the bandwidth limitations of wave paddle means that a full broad banded spectrum cannot be generated. As suggested by the results in this article, this could lead to an increased number of rogue waves and an overestimate of the extreme loads recorded in model tests. This issue will be most significant for steep sea states. However, more research is needed on this topic to determine clear practical rules for industry. Currently, however, it is not possible to provide exact criteria and can only encourage those conducting experiments in severe directional seas to be cautious in interpreting results.

Acknowledgment

D.B. has been supported by a studentship from the Engineering and Physical Sciences Research Council (EPSRC) of the UK Government. T.S.vd.B. acknowledges a Royal Academy of Engineering Research Fellowship.

Conflict of Interest

There are no conflicts of interest.

Data Availability Statement

The datasets generated and supporting the findings of this article are obtainable from the corresponding author upon reasonable request.

References

[1] Fedele, F., Brennan, J., De León, S. P., Dudley, J., and Dias, F., 2016, "Real World Ocean Rogue Waves Explained Without the Modulational Instability," Sci. Rep., **6**, p. 27715.
[2] Janssen, P. A. E. M., 2003, "Nonlinear Four-Wave Interactions and Freak Waves," J. Phys. Oceanogr., **33**, pp. 863–884.
[3] Kharif, C., and Pelinovsky, E., 2003, "Physical Mechanisms of the Rogue Wave Phenomenon," Eur. J. Mech. B/Fluids, **22**, pp. 603–634.
[4] Kharif, C., Pelinovsky, E., and Slunyaev, A., 2008, *Rogue Waves in the Ocean*, Springer Science & Business Media, Berlin, Germany.
[5] Dysthe, K., Krogstad, H. E., and Müller, P., 2008, "Oceanic Rogue Waves," Annu. Rev. Fluid Mech., **40**, pp. 287–310.
[6] Adcock, T. A. A., and Taylor, P. H., 2014, "The Physics of Anomalous ('Rogue') Ocean Waves," Rep. Prog. Phys., **77**, p. 105901.
[7] Mori, N., and Janssen, P. A. E. M., 2006, "On Kurtosis and Occurrence Probability of Freak Waves," J. Phys. Oceanogr., **36**(7), pp. 1471–1483.
[8] Dalzell, J. F., 1999, "A Note on Finite Depth Second-Order Wave–Wave Interactions," Appl. Ocean Res., **21**(3), pp. 105–111.
[9] Madsen, P. A., and Fuhrman, D. R., 2012, "Third-Order Theory for Multi-directional Irregular Waves," J. Fluid Mech., **698**, pp. 304–334.
[10] Fedele, F., 2015, "On the Kurtosis of Deep-Water Gravity Waves," J. Fluid Mech., **782**, pp. 25–36.
[11] Janssen, P. A. E. M., and Bidlot, J. R., 2009, "On the Extension of the Freak Wave Warning System and Its Verification," *ECMWF Tech. Mem.* 588. ECMWF.
[12] Mori, N., Onorato, M., and Janssen, P. A. E. M., 2011, "On the Estimation of the Kurtosis in Directional Sea States for Freak Wave Forecasting," J. Phys. Oceanogr., **41**(8), pp. 1484–1497.
[13] Onorato, M., Cavaleri, L., Fouques, S., Gramstad, O., Janssen, P. A., Monbaliu, J., Osborne, A. R., Packozdi, C., Serio, M., Stansberg, C. T., and Toffoli, A., 2009, "Statistical Properties of Mechanically Generated Surface Gravity Waves: A Laboratory Experiment in a Three-Dimensional Wave Basin," J. Fluid Mech., **627**, pp. 235–257.
[14] Toffoli, A., Gramstad, O., Trulsen, K., Monbaliu, J., Bitner-Gregersen, E., and Onorato, M., 2010, "Evolution of Weakly Nonlinear Random Directional Waves: Laboratory Experiments and Numerical Simulations," J. Fluid Mech., **664**, p. 313.
[15] Xiao, W., Liu, Y., Wu, G., and Yue, D. K., 2013, "Rogue Wave Occurrence and Dynamics by Direct Simulations of Nonlinear Wave-Field Evolution," J. Fluid Mech., **720**, p. 357.
[16] Trulsen, K., Kliakhandler, I., Dysthe, K. B., and Velarde, M. G., 2000, "On Weakly Nonlinear Modulation of Waves on Deep Water," Phys. Fluids, **12**(10), pp. 2432–2437.
[17] Trulsen, K., 2018, "Rogue Waves in the Ocean, the Role of Modulational Instability, and Abrupt Changes of Environmental Conditions that Can Provoke Non Equilibrium Wave Dynamics," *The Ocean in Motion*, M. Velarde, R. Tarakanov, and A. Marchenko, eds., Springer Oceanography, Springer AG.
[18] Waseda, T., Toba, Y., and Tulin, M. P., 2001, "Adjustment of Wind Waves to Sudden Changes of Wind Speed," J. Oceanogr., **57**, pp. 519–533.
[19] Viotti, C., and Dias, F., 2014, "Extreme Waves Induced by Strong Depth Transitions: Fully Nonlinear Results," Phys. Fluids, **26**(5), p. 051705.
[20] Rapizo, H., Waseda, T., Babanin, A. V., and Toffoli, A., 2016, "Laboratory Experiments on the Effects of a Variable Current Field on the Spectral Geometry of Water Waves," J. Phys. Oceanogr., **46**(9), pp. 2695–2717.
[21] Barratt, D., Bingham, H. B., Taylor, P. H., Van Den Bremer, T. S., and Adcock, T. A. A., 2021, "Rapid Spectral Evolution of Steep Surface Wave Groups With Directional Spreading," J. Fluid Mech., **907**, p. A30.
[22] Waseda, T., Kinoshita, T., Cavaleri, L., and Toffoli, A., 2015, "Third-Order Resonant Wave Interactions Under the Influence of Background Current Fields," J. Fluid Mech., **784**, pp. 51–73.
[23] Toffoli, A., Bennetts, L. G., Meylan, M. H., Cavaliere, C., Alberello, A., Elsnab, J., and Monty, J. P., 2015, "Sea Ice Floes Dissipate the Energy of Steep Ocean Waves," Geophys. Res. Lett., **42**(20), pp. 8547–8554.
[24] Meylan, M. H., Bennetts, L. G., Mosig, J. E. M., Rogers, W. E., Doble, M. J., and Peter, M. A., 2018, "Dispersion Relations, Power Laws, and Energy Loss for Waves in the Marginal Ice Zone," J. Geophys. Res., **123**(5), pp. 3322–3335.
[25] Dysthe, K. B., Trulsen, K., Krogstad, H. E., and Socquet-juglard, H., 2003, "Evolution of a Narrow-band Spectrum of Random Surface Gravity Waves," J. Fluid Mech., **478**, pp. 1–10.
[26] Osborne, A., 2010, *Nonlinear Ocean Waves and the Inverse Scattering Transform*, Academic Press, New York.
[27] Trulsen, K., and Dysthe, K. B., 1996, "A Modified Nonlinear Schrödinger Equation for Broader Bandwidth Gravity Waves on Deep Water," Wave Motion, **24**(3), pp. 281–289.
[28] Martin, D. U., and Yuen, H. C., 1980, "Quasi-Recurring Energy Leakage in the Two-Space-Dimensional Nonlinear Schrödinger Equation," Phys. Fluids, **23**, pp. 881–883.
[29] Yuen, H. C., and Lake, B. M., 1980, "Instabilities of Waves on Deep Water," Ann. Rev. Fluid Mech., **12**, pp. 303–334.
[30] Barratt, D., and Adcock, T. A. A., 2021, "MNLS Simulations of Surface Wave Groups With Directional Spreading in Deep and Finite Depth Waters," J. Ocean Eng. Mar. Energy, **7**, pp. 1–15.
[31] Adcock, T. A. A., and Taylor, P. H., 2016, "Fast and Local Non-linear Evolution of Steep Wave-Groups on Deep Water: A Comparison of Approximate Models to Fully Non-Linear Simulations," Phys. Fluids., **28**(1), p. 016601.
[32] Adcock, T. A. A., and Taylor, P. H., 2016, "Non-linear Evolution of Uni-directional Focussed Wave-groups on a Deep Water: A Comparison of Models," Appl. Ocean. Res., **59**, pp. 147–152.
[33] Janssen, P. A. E. M., 1983, "On a Fourth-Order Envelope Equation for Deep-Water Waves," J. Fluid Mech., **126**, pp. 1–11.
[34] Zakharov, V. E., and Shabat, A. B., 1972, "Exact Theory of Two-Dimensional Self-Focusing and One-Dimensional Self-Modulation of Waves in Nonlinear Media," Soviet Phys. JETP, **34**, pp. 62–69.
[35] Serio, M., Onorato, M., Osborne, A. R., and Janssen, P. A., 2005, "On the Computation of the Benjamin-Feir Index," Nuovo Cimento, **28**(6), pp. 893–903.
[36] Young, I. R., 1995, "The Determination of Confidence Limits Associated With Estimates of the Spectral Peak Frequency," Ocean Eng., **22**(7), pp. 669–686.
[37] Goda, Y., 1985, *Random Seas and Design of Marine Structures*, University of Tokyo Press, Tokyo, Japan, p. 239.